Original Article

Evaluation of the effect of co-transplantation of collagen-hydroxyapatite bio-scaffold containing nanolycopene and human endometrial mesenchymal stem cell derived exosomes to regenerate bone in rat critical size calvarial defect

Masoumeh Einabadi [a], Azadeh Izadyari Aghmiuni [b], Laleh Foroutani [b], Arman Ai [b], Mojdeh Salehi Namini [a], Ali Farzin [c], Amir Nahanmoghadam [d], Sadegh Shirian [e], Hossein Kargar Jahromi [f, *], Jafar Ai [a, **]

[a] Department of Tissue Engineering, School of Advanced Technologies in Medicine, Tehran University of Medical Sciences, Tehran, Iran
[b] School of Medicine, Tehran University of Medical Sciences, Tehran, Iran
[c] Department of Applied Cell Sciences, School of Advanced Technologies in Medicine, Tehran University of Medical Sciences, Tehran, Iran
[d] Department of Chemical Engineering, Faculty of Engineering, Shiraz Branch, Islamic Azad University, Shiraz, Iran
[e] Department of Pathology, School of Veterinary Pathology, Shahrekord University, Shahrekord, Iran
[f] Research Center for Noncommunicable Diseases, Jahrom University of Medical Sciences, Jahrom, Iran

ARTICLE INFO

ABSTRACT

This study aimed to evaluate the effect of nanoparticles based on the PLGA and biomolecule of lycopene (i.e. NLcp) and exosomes loaded on hydroxyapatite/collagen-based scaffolds (HA/Coll), on human endometrial MSCs (hEnMSCs) differentiation into osteoblast cells. To this end, after synthesizing NLcp and isolating hEnMSC-derived exosomes, and studying their characterizations, HA/Coll scaffold with/without NLcp and exosome was fabricated. In following, the rat skull-defect model was created on 54 male Sprague−Dawley rats (12 weeks old) which were classified into 6 groups [control group (4 healthy rats), negative control group: bone defect without grafting (10 rats), and experimental groups including bone defect grafted with HA/Coll scaffold (10 rats), HA/Coll/NLcp scaffold (10 rats), HA/Coll scaffold + exosome (10 rats), and HA/Coll-NLcp scaffold + exosome (10 rats)]. Finally, the grafted membrane along with its surrounding tissues was removed at 90 days after surgery, to assess the amount of defect repair by Hematoxylin and eosin staining. Moreover, immunohistochemical and X-ray Micro-Computed Tomography (Micro-CT) analyses were performed to assess osteocalcin and mean bone volume fraction (BVF). Based on the results, although, the existence of the exosome in the scaffold network can significantly increase mean BVF compared to HA/Coll scaffold and HA/Coll-NLcp scaffold (2.25-fold and 1.5-fold, respectively). However, the combination of NLcp and exosome indicated more effect on mean BVF; so that the HA/Coll-NLcp scaffold + exosome led to a 15.95 % increase in mean BVF than the HA/Coll scaffold + exosome. Hence, synthesized NLcp in this study can act as a suitable bioactive to stimulate the osteogenic, promotion of cell proliferation and its differentiation when used in the polymer scaffold structure or loaded into polymeric carriers containing the exosome.

© 2024 The Author(s). Published by Elsevier BV on behalf of The Japanese Society for Regenerative Medicine. This is an open access article under the CC BY-NC-ND license (http://creativecommons.org/licenses/by-nc-nd/4.0/).

* Corresponding author. Research Center for Noncommunicable Diseases, Jahrom University of Medical Sciences, Jahrom, Iran.
** Corresponding author. Department of Tissue Engineering, School of Advanced Technologies in Medicine, Tehran University of Medical Sciences, Tehran, Iran.
E-mail addresses: hossein.kargarjahromy@gmail.com (H. Kargar Jahromi), jafar_ai@tums.ac.ir (J. Ai).
Peer review under responsibility of the Japanese Society for Regenerative Medicine.

1. Introduction

Nowadays, large bone defects caused by trauma, tumors, periodontal diseases, and other diseases are very common [1,2]. However, the partial or large-area resection of such bones to treat or reconstruct the lesion is still considered a major challenge, due to poor regeneration, nonunion, or delayed healing [1−5]. Generally,

xenografts, allografts, and autografts are used in this field, clinically. Although, autologous bone grafting is known as the "gold standard" to repair large bone defects due to better osteoconduction, osteogenesis, and osteoinduction [6—8]. However, there are major problems with the use of these grafts, including limitations of donor sites and complicated shape/size of damaged bone, donor site morbidity for patients such as long re-habilitation time, poor recovery of bone postoperative, and additional pains caused by the created bone lesion at extraction site [1,2,4].

In recent years, novel strategies based on tissue engineering have provided promising paths for the treatment or regeneration of bone-related diseases [9]. Such that, today, the use of bone tissue-engineered scaffolds has developed as a new substitute for damaged tissue [1]. However, the selection of suitable materials and then design and/or optimization of scaffold possess the important clinical significance; because the effective repair depends on the interaction of the cell-scaffold and regulation of cellular behavior, as well as the scaffold properties (biodegradability, biocompatibility, mechanical stability, low-level immune response, hydrophilicity, etc.) [10—13].

Polyester PLGA is one of the attractive copolymers in this field that ability to control degradation rate and high flexibility to add cell-binding peptides and results in an increase in biomimetic properties of scaffold [14—16]. Although, bio-incompatibility and poor cell adhesion are known as the most important disadvantages of this copolymer [16].

Based on the reports, the design of hybrid or composite scaffolds can significantly decrease the disadvantages of single-polymer scaffolds. Collagen is a sample of these polymers that can help to biological and physiological functions of the cell and scaffold as a dynamic bio-material [17—19]. In this field, Shih et al. reported that collagen fibrous mats can be led to an increase in the growth, proliferation, adhesion, and osteogenic differentiation of human-MSCs [20].

Hydroxyapatite also is a natural mineral form that can mimic natural bone constitution in the scaffold network and be led to an increase in osteocalcin expression and osteogenesis, as well as improvement of stem cell proliferation, mineral deposition, and osteogenic differentiation.

Although the substrates based on the hydroxyapatite and nanohydroxyapatite-collagen can be used in regenerating bone and cartilage [21,22], however, studies have shown that the use of bioactive or herbal active ingredients, in the scaffold/substrate structure, can promote the rates of the cell differentiation and the bone tissue regeneration.

Cissus quadrangularis [23], *Helminthostachys zeylanica* L. [24], *Herba epimedii* [25], Neobavaisoflavone in *Psoralea corylifolia* L. [26], the biomolecules of lycopene, quercetin and rutin in Fruit and vegetables [27,28], etc. are samples of bioactive materials that can be led to a stimulation of osteogenic, promotion of cell proliferation and mineralization, formation of bone nodules, and the increase in the expression of bone-specific matrix proteins like collagen I, bone sialoprotein, and osteocalcin when used in the polymer scaffold structure or loaded into polymeric carriers.

Moreover, mesenchymal stem cells (MSCs) have illustrated to be a valuable sources for cell-based therapies in regenerative medicine such as the regeneration of bone tissues [29,30], although, engraftment at the injury site is poor. In recent years, it has been recorded that MSCs can act through the paracrine signaling mechanisms. In this regard, exosomes as the nano-biostructures play an important role. They can carry DNAs, RNAs, proteins, and lipids, as well as, improve cell-to-cell interactions. Based on the studies, these attractive nanostructures, in a bone microenvironment can promote in *vivo*/in *vitro* osteogenesis and osteogenic differentiation [31—33]. Hence, the engineered scaffold design can

be an effective factor in improving the function of these nanostructures.

Accordingly, this research aimed to assess the role of hydroxyapatite-collagen bio-scaffold loaded with nanoparticles (NLcp) based on PLGA (as carrier) and lycopene (as bioactive molecule) and exosomes, in human endometrial MSCs (hEnMSCs) differentiation into osteoblast cells. To study this effect, the rat skull-defect model was created on 54 male Sprague—Dawley rats (12-weeks old) [6 groups: 4 rats in the control group, and 10 rats in the negative control and experimental groups]. Notably, the experimental groups included HA/Coll scaffold (10 rats), HA/Coll/NLcp scaffold (10 rats), HA/Coll scaffold + exosome (10 rats), and HA/Coll/NLcp scaffold + exosome (10 rats). Finally, the results of histopathological, Masson trichrome staining, immunohistochemistry staining, and X-ray Micro-Computed Tomography (Micro-CT) were analyzed on days 45 and 90 post-implantation.

2. Materials and methods

2.1. Materials

Hydroxyapatite (nano-powder with a particle size <200 nm, BET), ≥97%, synthetic), collagenase type I, and Ficoll were purchased from Sigma (Sigma—Aldrich Inc., St. Louis, MO, USA). Lycopene, PLGA, DMSO, PVA, ascorbic acid, Dexamethasone, Indomethacin, Oil red O stain, Alizarin red S solution, isopropyl alcohol, paraformaldehyde and formaldehyde, ethanol, β-Glycerol phosphate disodium salt, exosome isolation kit (Exocib C), ketamine hydrochloride, xylazine, acepromazine, lidocaine, ketoprofen, cefazolin were also obtained from Merck company (Germany).

Moreover, Hank's medium (HBSS; Invitrogen, Carlsbad, CA), PBS (phosphate-buffered saline), penicillin-streptomycin (Pen-Strep), DMEM-F12 medium, FBS (fetal bovine serum), BSA (bovine serum albumin), were purchased from Gibco (Massachusetts, USA), as well as, anti-CD105, anti-CD-90, anti-CD-146, anti-CD-34, and anti-CD31 were also obtained from Abcam Company (Cambridge, UK). Likewise, primary anti-CD63 monoclonal antibody and secondary horseradish peroxidase (HRP)-conjugated antibody were purchased from Santa Cruz Biotechnology (Dallas, Texas, USA) and SinaClon (Tehran, Iran), respectively.

2.2. Preparation and characterization of nano-lycopene

The precipitation method was used to synthesize PLGA-Lycopene nanoparticles. Briefly, PLGA (50 mg) along with lycopene (10 mg) was dissolved in 5 ml DMSO. This solution was then added to 100 ml aqueous phase solution containing 1% (w/v) PVA and stirred at 25 °C for 12 h (500 rpm), to evaporate the organic phase. Afterward, the solution was centrifuged (12,000 g, 20 min) to separate the nanoparticles and washed 3 times with distilled water to remove the remaining surfactant. The mentioned suspension was frozen (−80 °C, 8 h) and then freeze-dried at −40 °C, for 24 h; finally, the characterization of nanoparticles was assessed. Notably, the supernatant was analyzed to measure the amount of free-drug.

In the following, the chemical characterization of nanoparticles and biomolecule of lycopene and carrier of PLGA were studied by Fourier Transform Infrared Spectroscopy (FTIR-spectrum analysis, Model-ALPHA, Bruker, Germany). The encapsulation percentage of lycopene into nanoparticles was also studied by the determination of the EE% (encapsulation efficiency%) and DL% (drug loading%). To this end, ultraviolet—visible (UV) light absorbance of the centrifuge-obtained supernatant was measured by an UV—visible spectrophotometer (Optizeri2120 UV-plus) at 470 nm, by quartz cuvettes. Then, the calibration curve of biomolecule (i.e. lycopene)

was obtained by preparing different concentrations of lycopene into DMSO (0.1–3 mg/ml) and measuring the absorbance of these solutions, to determine free lycopene concentration into the supernatant. Finally, EE (%) and DL (%) were calculated by Eqs. (1) and (2).

$$EE\,(\%) = [(\text{total drug} - \text{amount of drug into supernatant}) \\ / \,\text{amount of total drug}] \times 100 \quad (1)$$

$$DL\,(\%) = [(\text{total drug} - \text{amount of drug into supernatant}) \\ / \,(\text{total weight of polymer} + \text{total drug}] \times 100 \\ (2)$$

Moreover, to study in-vitro release profile of the biomolecule of lycopene, 10 mg of lycopene-loaded nanoparticles (freeze-dried) was dispersed into a 5 ml solution of PBS: Tween-80 (0.01% w/v). The mentioned suspension was dialyzed against 50 ml of the same solution (pH; 7.4) with a dialysis sac (MWCO: 12,000 Da) at 37 °C, for 240 h. The PBS: Tween-80 solution (3 ml) was also replaced with the equal volume of fresh solution, at predetermined time intervals. Finally, the amount of drug released from nanoparticles and its release behavior was assessed with UV measurement (at 470 nm) and the use of a calibration curve.

Moreover, the zeta potentials and mean diameter (Dm) of nanoparticles were studied at 25 °C by a DLS (dynamic light scattering) instrument with ZetaSizer (Nano-ZS) (Malvern Instruments, Worcestershire, UK) with an argon laser beam at 633 nm and 90° scattering angle, refractive index: 1.49, and absorbance of the polymer at the 0.0. The morphology and size nanoparticles were also assessed a the FESEM (scanning electron microscope, XL30 ESEM, Germany), n = 100.

2.3. Fabrication of scaffold with/without nanoparticle

Collagen slurry (0.5% w/v) was obtained by adding its dry powder to glacial acetic acid (0.05 M). Then, hydroxyapatite (HA) was added to this slurry (80:20 w/w) under stirring conditions. The slurry was poured into cylindrical silicone molds, and the molds lyophilized into a freeze drier (Telstar Lyo Quest 55 plus) at −50 °C (3 °C/min) and for 72 h. The HA-Collagen (HA/Coll) sponges as controls were fabricated by freeze-drying.

Likewise, hydroxyapatite (HA), collagen (Coll), and nano-lycopene (NLcp) were combined with the weight ratio of 80/20/1 (HA/Coll/NLcp), to prepare nanoparticle doped sponges. To this end, HA and NLcp were first mixed in a porcelain mortar and ground thoroughly. Afterward, the scaffolds were fabricated by adding the HA/NLcp particles to the collagen slurry under a vigorous stirring process before the freeze-drying stage and then dried under conditions similar to the process previously mentioned for HA-collagen. To reduce solubility in water, sponges were cross-linked with 3% (w/v) glutaraldehyde vapor for 24 h. Finally, the characterization of composite sponges was studied for use as a potential bone substitute.

2.4. Chemical characterization by FTIR

The surface chemistry study and FTIR spectroscopic analysis of designed scaffolds and their materials were carried out determined by Fourier Transform Infrared Spectroscopy (FTIR-spectrum analysis, Model-ALPHA, Bruker, Germany) [wavenumber range: 450–4000 cm^{-1}, a resolution of 4 cm^{-1}]. Briefly, the samples were mixed with potassium bromide at a 1:1 ratio, pressed into a pellet, and then their spectra were measured by FTIR-spectrum analysis.

2.5. Mechanical behavior

To perform the Compressive mechanical test, the diameter and height of the scaffold were determined by the digital caliper gauge, and then the mechanical behavior of the scaffold was measured on a Universal Tester, Instron 4204 (Norwood) which was equipped with a static 1 kN load cell (Instron 2525 series), and 50 mm compression platens. Afterward, the scaffold was compressed to 40% of its initial height at the rate of 2 mm/min. Finally, elastic modulus, σ yield, and ε failure were determined in triplicate.

2.6. Microstructural observation

The morphology assessment of the scaffold was observed by a scanning electron microscope (SEM) (XL30 ESEM, Philips, Germany). To this end, the samples were imaged at the accelerating voltage of 25.0 kV, and then the surface morphology of the scaffold was analyzed by Clemex Vision software.

Likewise, the NLcp morphology was studied by field emission scanning electron microscopy (FESEM, Carl Zeiss FE-SEM SUPRA 35 VP). Briefly, the sample was pressed onto the double-sided carbon adhesive tape and surface morphology and pore sizes of samples were assessed in the acceleration voltage of 1 kV and analyzed by Clemex Vision software.

2.7. Isolation of human endometrial MSCs (hEnMSCs)

Isolation of hEnMSCs was performed according to the described method by Heidari-Keshel et al. [34]. In Brief, endometrial tissue was obtained with informed consent from patients who went to the Imam Khomeini Hospital (Tehran, Iran) for infertility treatment. All experiments and protocols of this study were approved by the Ethics Committee of Tehran University of Medical Science.

The endometrial tissues were placed in Hank's medium and delivered to the cell culture laboratory. Afterward, the specimens were washed with PBS containing 1% Pen-Strep and then incubated into 2 mg/mL collagenase type I at 37 °C (5% CO2) for 2 h to digest tissue. Followed by, the suspension was passed by cell strainers of 70 μm and 40 μm, respectively. Then, Ficoll (Sigma, USA) was used to remove the mononuclear cells. Afterward, the isolated cells were transferred to DMEM-F12 containing 15% FBS and 1% Pen-Strep. Finally, the differentiation characterization and surface markers of these cells (hEnMSCs) were studied after passage 3.

2.8. Immunophenotype of hEnMSC by flow cytometric

A Flow Cytometric test was performed to study hEnMSC surface markers. Notably, the immunophenotype of hEnMSCs in terms of the expression of MSC surface markers was assessed according to the indexes of the International society of cell therapy.

Briefly, the suspension of hEnMSC (passage 3) was added to each vial containing antibodies of anti-CD105, anti-CD-90, anti-CD-146, anti-CD-34, and anti-CD31 (Abcam Co., Cambridge, UK) and then incubated for 1 h (4 °C). Finally, cells were fixed in 100 μl paraformaldehyde (1%), and the statistical record was analyzed by the Becton Dickinson device (BD Biosciences CA, USA) and flowing software 2.5.1. Notably, data were calculated and expressed as mean ± SD, n = 3.

2.9. Evaluation of hEnMSC differentiation into adipose cells

To differentiate hEnMSCs into adipose cells, passages 3–4 of hEnMSCs (at the concentration of 2×10^4 cells/well) were cultured in DMEM-F12 supplemented with 10% FBS.

When the cells were 70–80% confluent, the DMEM-F12 medium was replaced with a differentiation medium of adipogenic, and the cells were treated with the mentioned medium for 3 weeks. The control sample (i.e.un-differentiation cells) was also cultured in DMEM-F12 containing 2% FBS, for 21 days. Then adipose drops (no staining) were observed by phase contrast microscopy.

Notably, the differentiation medium of adipogenic was included DMEM-F12 containing FBS (2%), ascorbic acid (50 μg/ml), dexamethasone (10^{-7} Molar), and indomethacin (50 μg/ml).

Moreover, the cells were stained by the Oil red O method to evaluate hEnMSCs differentiation into adipose cells. To this end, 0.5 g oil red powder was dissolved in 100 ml isopropyl alcohol (99%). This solution was added to distilled water (2:3 v/v) and filtered after 15 min. Following, cells were fixed in paraformaldehyde (4%), at room temperature for 1 h and then washed with ethanol (70%). Afterward, the staining was performed with Oil red O solution (0.5%), at 25 °C, for 10–15 min. Finally, the differentiated cells were observed by inverted microscopy.

2.10. Evaluation of hEnMSCs differentiation into osteoblast cells

To differentiate hEnMSCs into osteoblast cells, passages 3–4 of hEnMSCs (at the concentration of 2×10^4 cells/well) were cultured in DMEM-F12 supplemented with 10% FBS. When the cells were 80–90% confluent, the DMEM-F12 medium was replaced with a differentiation medium of osteogenic, and the cells were treated with the mentioned medium for 21 days. The control sample (i.e. un-differentiation cells) was also cultured in DMEM-F12 containing 2% FBS, for 21 days. Finally, the cell staining was performed by Alizarin red S staining protocol. Briefly, the cell monolayer was washed with PBS solution, then, the cells were fixed with methanol (25 °C), stained with Alizarin red S solution (1% in 25% ammonia solution) for 2 min, and observed by inverted microscopy.

Notably, the differentiation medium of osteogenic was included DMEM-F12 containing FBS (2%), ascorbic acid (50 μg/ml), dexamethasone (10^{-8} Molar), and β-Glycerol phosphate disodium salt (10 mMolar).

2.11. Isolation and characterization of hEnMSC-derived exosomes

The passage-3 of mesenchymal stem cells were cultured into DMEM containing FBS (10%), penicillin 100 U/ml-streptomycin 100 μg/ml, at 37 °C, and 5% CO_2. When the cells were more than 80% confluent, the cells were cultured into a culture medium (serum-free) for 48 h. The exosomes were isolated from the hEnMSC culture supernatant at 70% < confluence. To this end, the supernatant was centrifuged at 300×g (10 min). Afterward, the cell suspension was re-centrifuged at 2000×g (10 min) and then 10,000×g (30 min) to remove dead cells, cell debris, and large particles. Finally, the exosomal pellet was obtained by an exosome isolation kit (Exocib C). Then, the hEnMSC- obtained exosome pellets were suspended in PBS and their characterization was analyzed, such as the determination of exosome concentration, exosome size, morphology, and Immunophenotype of the exosome.

2.12. Determination of exosome characterization

Bradford assay was performed to determine the concentration of exosomes. To this end, the different concentrations of bovine serum albumin (BSA) were prepared and 10 μl of each concentration was added to a 6-well plate containing Bradford solution (200 μl), separately. Afterward, absorbance was measured at a wavelength of 595 nm, and the concentration of exosomes was determined via a standard curve.

Moreover, the DLS measurement was performed to study the size distribution of exosomes by dynamic light scattering with a Zetasizer Nano ZS. To this end, 50 μl exosomes were diluted into PBS (950 μl), and then the sample was measured with the standard setting (absorption: 0.01, refraction: 1.38°, and temperature of the Holder = 25 °C).

To observe the morphology and particle size of exosomes, scanning electron microscopy (SEM, KYKY-Digital SEM M3200). Briefly, 10 μl of the diluted suspension of exosome was poured on a glass slide. After 24 h, the sample was observed by SEM (accelerating voltage: 25.0 kV).

Followed by, Western blotting analysis was carried out to assess the exosomal marker protein CD63. To this end, proteins were transferred to a nitrocellulose membrane, after extraction and separation of total exosomal proteins using RIPA buffer (radio-immunoprecipitation assay) and 12% sodium dodecyl sulfate-polyacrylamide gel electrophoresis (SDS-PAGE), respectively. The membrane was blocked with blocking solution (5% milk and 0.05% Tween-20 in PBS) at room temperature for 24 h and incubated with primary anti-CD63 monoclonal antibody for 2.5 h. Afterward, the membrane was washed three times with PBS, then incubated with secondary horseradish peroxidase (HRP)-conjugated antibody at room temperature, for 2 h, and washed twice with PBS. Finally, the bands were visualized using a chemiluminescent detection system.

2.13. HEnMSC-derived exosomes-loaded scaffolds

The designed scaffolds were placed in 6-well plates and covered by HEnMSC-derived exosomes (200 μg/ml). Afterward, the samples were incubated at 37 °C, for 4 h, and then the physicochemical and biological properties of scaffolds were studied to assess parameters of biocompatibility and degradation.

To assess biocompatibility, 5×10^4 cells/well were seeded onto the 96-well plates containing hEnMSC-derived exosomes-loaded scaffolds and an MTT assay was performed after 1, 3, and 7 h of culture. To this end, after removing the culture medium, the MTT (10 μl, 5 mg/mL concentration) was added to each well. After 4 h of incubation and removal of the medium, the cells were dissolved in DMSO (dimethyl sulfoxide, 200 μl); finally, their absorbance was measured at the wavelength of 570 nm (100% cell viability: control group).

The degradation rate of the scaffolds was also determined by measuring the weight loss of designed scaffolds for 90 days. Briefly, the samples were soaked in 10 mL phosphate buffer saline with a PH of 7.4 and all the samples were incubated at 37 °C for 15, 30, 60, and 90 days. The weight loss was calculated by using Eq. (3), where W1 and W2 are the initial weight and secondary weight of samples (i.e. after taken out of PBS and then freeze-dried for 24 h), respectively. The average data were reported for each of the samples using three measurements.

$$\text{Weight Loss} = \frac{W1 - W2}{W1} \times 100 \qquad (3)$$

2.14. Release of scaffold-encapsulated exosomes

The release of HEnMSC-derived exosomes from the designed scaffolds was assessed in PBS solution (0.1 M, pH 7.2). To this end, 5 mg of scaffolds containing exosomes were immersed in PBS (2 ml) and then incubated at 37 °C and designated time points (hours 1, 4, 8, 14, 24, 36, 48, and 72, as well as, days 7, 15, 30, 60, 90). At the end of each period, the PBS solution was removed, scaffolds were frozen at −80 °C, and fresh PBS solution was replaced after each analysis. Finally, the cumulative release of exosomes was determined by Eq. (4)

$$Cumulative\ Release\% = \frac{W_{entraped\ exosomes(t)}}{W_{encapsulated\ exosomes}} \times 100 \qquad \text{Eq. (4)}$$

2.15. Animal experiments

The experimental protocols and the use of animals were approved by the Animal Research Committee of Jahrom University School of Medicine and the procedure was based on the guide of the care/use of laboratory animals published by the National Academy of Sciences (ethical code: IR. JUMS.REC.1399.164). The surgeries were carried out on 54 male Sprague—Dawley rats (12 weeks old). The rats were randomly distributed into 6 groups (4 rats in the control group, and 10 rats in the negative control and experimental groups, separately). Notably, 5 groups were examined as experimental groups, as well as, the surgery was performed without grafting in the negative control group.

Briefly, the disk was prepared and impregnated with exosomes to implant in the skull of the rat. Then, the bone defect (8 mm) was made in calvarium and grafted with the collagen-based membrane on the site. To this end, rats were anesthetized by administration of the anaesthesia mixture containing 60 mg/kg ketamine hydrochloride, 10 mg/kg xylazine, and acepromazine (3 mg/kg). To control the pain during surgery, 2% lidocaine hydrochloride (local anaesthetic) was administered. Moreover, ketoprofen (5 mg/kg) and cefazolin (20 mg/kg) were administered to control pain and infection after surgery, respectively.

Finally, the grafted membrane along with its surrounding tissues was removed at 45 and 90 days after surgery, to assess the amount of defect repair by Hematoxylin and eosin staining. In brief, at 45 and 90 days after the surgery, from each group, the 4 rats were sacrificed (control group: 2 rats were sacrificed) via euthanasia with ketamine (150 mg/kg) and xylazine (20 mg/kg) and then their skull were dissected and placed in 10% formalin buffer solution. After fixing, decalcification, dehydration, and molding with paraffin, a 5 cm-thickness incision was made in the central part of the samples by microtome. The incisions were stained by Hematoxylin and eosin method and then assessed by the optical microscope. Moreover, immunohistochemical analyses were performed to assess osteocalcin.

The groups were as follows

1. Control group (4 healthy rats)
2. Negative control group: bone defect without grafting (10 rats)

    Experimental groups:

3. Bone defect grafted with HA/Coll scaffold (10 rats)
4. Bone defect grafted with HA/Coll-NLcp scaffold (10 rats)
5. Bone defect grafted with HA/Coll scaffold + exosome (10 rats)
6. Bone defect grafted with HA/Coll-NLcp scaffold + exosome (10 rats)

2.16. Micro-CT study

To quantitatively/qualitatively assess the formation of new bone and compared mean bone volume fraction (BVF), an in vivo X-ray Micro-Computed Tomography (Micro-CT) scanner (LOTUS-*in vivo*, Behin Negareh Co., Tehran, Iran) was carried out on all the groups.

In this assay, LOTUS-*in vivo* included a cone beam micro-focus X-ray source and a flat panel detector. To obtain the best quality of images, the X-ray tube voltage and its current were also set to 40 kV and 120 μA, respectively; as well as frame exposure time was set to 2 (sec) by 3.4 magnification. The total scan duration was 49 min. Slice thickness in reconstructed images was set to 35 μm. The protocol setting process was controlled via LOTUS-inVivo-ACQ software. The acquired 3D data was reconstructed using LOTUS inVivo-REC by a standard Feldkamp, Da-vis, Kress (FDK) algorithm. Moreover, LOTUS inVivo-3D was used for rendering reconstructed images. Bone Volume (BV) and Total Volume (TV) parameters were also reported by adding Bone Analysis Plugin (BAP) inside the software.

2.17. Statistical analysis

The experiments were cattied out at n = 3 and the values were described as the mean ± SD. Statistical analysis was carried out using the T-Test and one-way analysis of variance, LSD, and Tukey post hoc test in SPSS Statistics 24 software, and p < 0.05 were considered as statistically significant.

3. Result and discussion

3.1. Physicochemical and mechanical properties of nano-lycopene

Fig. 1A illustrates the FTIR spectra of the samples of lycopene, nano-lycopene (NLcp), and PLGA polymer. As observed in this figure, the recorded peak at the range of 640—655 cm^{-1} for the lycopene spectrum is related to CH=CH stretching vibration (green circle on the figure) [35], however, this peak has been removed in the NLcp spectrum that can be due to the interaction of polymer chains of PLGA with lycopene. Moreover, the peaks in the range of 1000—1060 cm^{-1} for the lycopene sample represent the trans-R—HC=CH—R [36]. Notably, the range change of the peaks and their intensity in the NLcp spectrum are attributed to chemical interactions between the polymer and lycopene. Likewise, the reduction in the intensity of peaks in the range of 1100—1250 cm^{-1} which is assigned to C—O asymmetric/symmetric stretching vibrations [37], as well as, the removal of some peaks at the range of 1960—2500 cm^{-1} (especially, the peak of 2062.68 cm^{-1} that assigned to C≡C symmetry stretching vibration [35]) was observed in NLcp spectrum than lycopene and PLGA spectra. It means that new bands were formed through the hydrogen bonds or electrostatic interaction in the inner/intermolecular of lycopene with polymer. The peaks in the range of 1300—1380 cm^{-1}, 1400-1450 cm^{-1}, and 1600-1650 cm^{-1} represent the —CH3 and -CH2 bonds, as well as, C=C aromatic stretching [37,38], respectively. The comparison of all three spectra in this range confirms the nanoparticle formation. Such changes (in terms of change in the intensity and location of peaks) were also observed in the range of 2800—3000 cm^{-1} and 3400-4000 cm^{-1} which assigned to asymmetric and symmetric stretching of the functional C—H bond and O—H stretch group, respectively [36,38—40].

Followed by, the comparison of the zeta potential of lycopene-loaded nanoparticles and lycopene demonstrated that zeta potential decreased from −29 mV (for free lycopene) to −9.3 mV (for NLcp) (Fig. 1B). Indeed, when lycopene was encapsulated into PLGA, the surface charge of nanoparticles changes; so that resulted in a higher electron dynamics within end groups of polymer that can create particles lower negatively charged than free lycopene. Based on the reports, surface charges lower than 5 mV lead to flocculation, conjugation, and consequently sedimentation as well as cause instability in colloids due to lack of repulsive forces [41,42].

Moreover, the DLS analysis results indicated that nanoparticles possess a mean diameter of 23.6 nm (Fig. 1C), while, the mean diameter obtained from FESEM was 19.71 nm ± 2.38, which can be due to the particle aggregation in the aqueous medium of DLS analysis [43] and/or measurement method of the hydrodynamic size in this technique. Such that hydrophilic polymer (as nano-carrier) extends and interacts with water, while dried
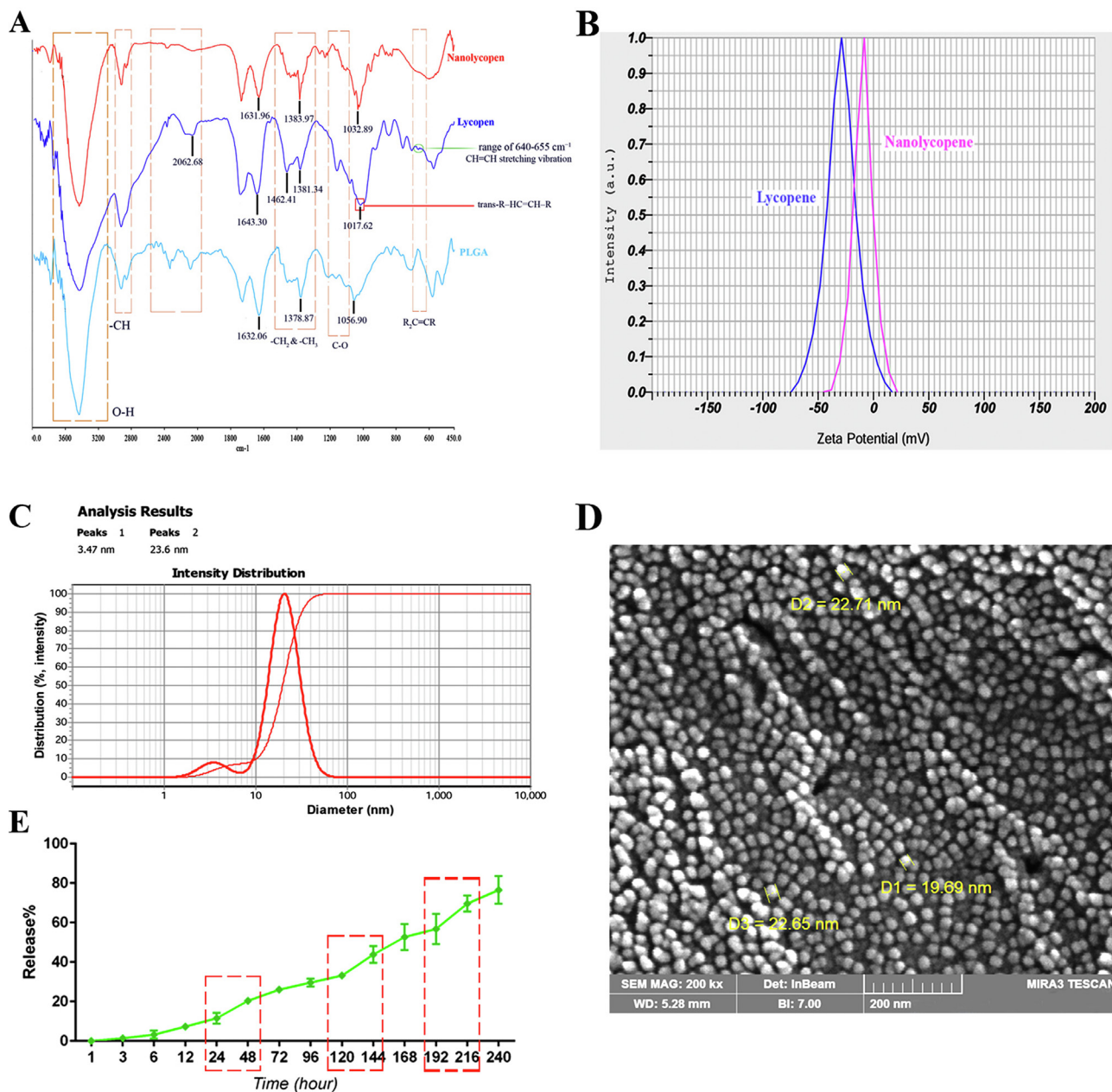
Fig. 1. FTIR spectra of samples (A), the zeta potential of lycopene-loaded nanoparticles and lycopene (B), DLS curve (C), FESEM images of nanoparticles (D), the curve of release profile (E).

nanoparticles are imaged in the FESEM analysis. Based on the FESEM images, nanoparticles possessed spherical, similar, and uniform morphology that can be owing to the suitable synthesis method for the preparation of these nanoparticles (Fig. 1D).

According to Eqs. (1) and (2), the encapsulation efficiency (%) and drug loading (%) were also measured. Based on the results, these values were equal to 85.0 % ± 3.06 and 22.0 % ± 0.29, respectively.

Furthermore, the study of release profile, into PBS: Tween 80 solution (pH 7.4) and at different times, indicated that the lycopene release from nanoparticles occurred over time (Fig. 1E). However, three explosive releases at intervals of 24−48 h, 120−144 h, and 192−216 h were observed in release profile of NLcp. Thus, it seems that the release of lycopene (as a biomolecule) from the nanoparticles possesses 2 types of release i.e. diffusion and

disintegration. This type of release can be related to the hydrophobic interactions between the lycopene and nanoparticle core or the swelling of the polymer/carrier shell [44].

3.2. Physicochemical and mechanical properties of scaffolds

Fig. 2A demonstrates the FTIR spectra for scaffolds of HA/Coll and HA/Coll-NLcp compared to the FTIR spectra of the samples of collagen, hydroxyapatite, and NLcp. As observed in the collagen spectrum, the band of N−H stretching at 3430.38 cm^{-1} is attributed to the amide A. Comparing collagen, hydroxyapatite, and HA/Coll spectra indicates that the shift of this band up to 3572.90 cm^{-1} in the HA/Coll spectrum is related to the interaction of hydroxyapatite chains with this functional group in collagen. Likewise, for the collagen spectrum, bands of C−H stretching at 2851.64 cm^{-1} and
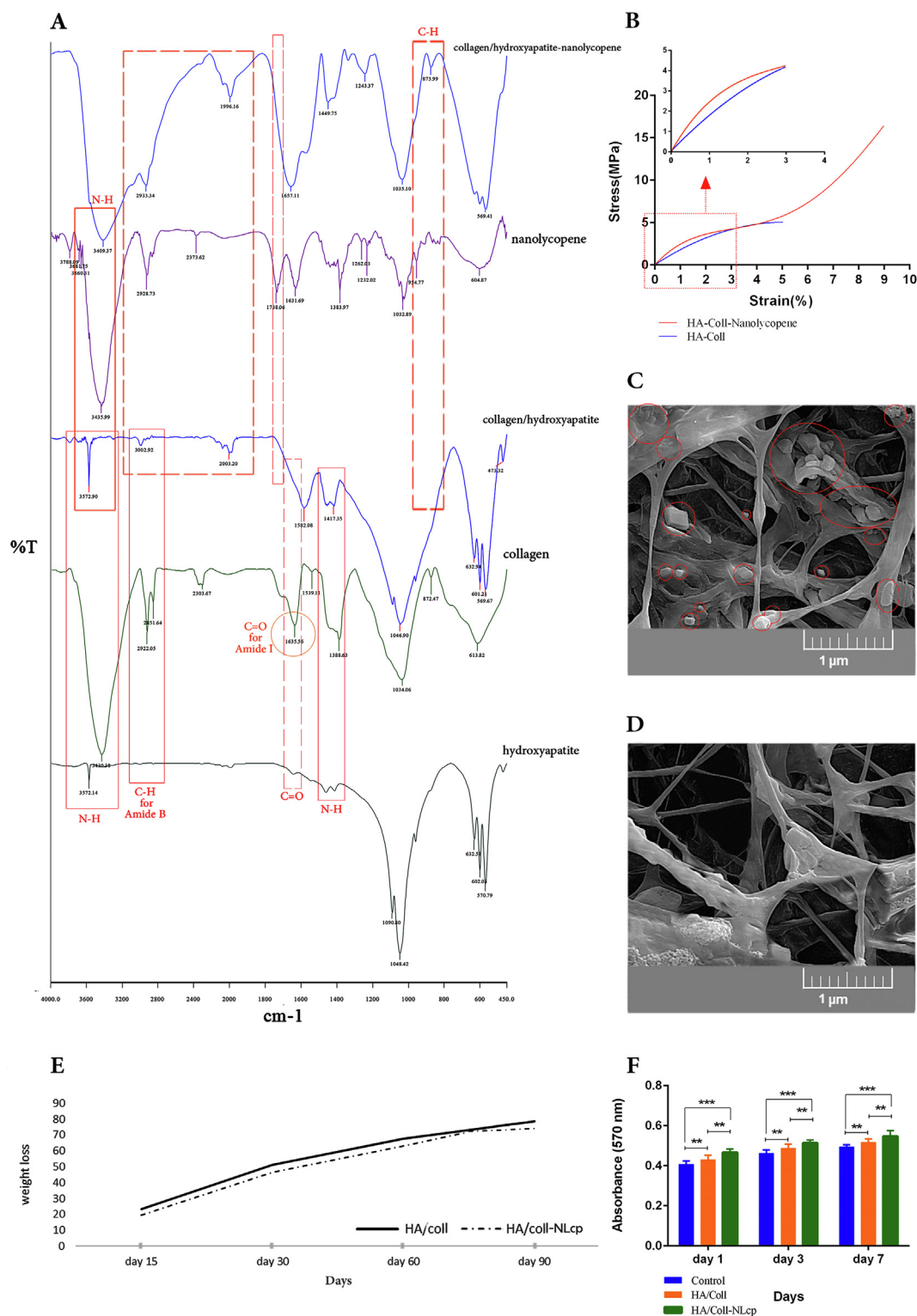
Fig. 2. FTIR spectra (A); the stress–stress curve of the HA/Coll-based scaffolds (B), SEM images of the designed scaffolds with (C) and without (D) nanoparticles; the degradation rate of scaffolds (black line: HA/coll, and dot-lined boxes: HA/coll-NLcp) (E); in-vitro cytotoxicity (F).

2922.05 cm^{-1}, C=O stretching at 1600–1700 cm^{-1} are related to amide B and amide I, respectively, that the change of their intensity and location in the spectrum of HA/Coll scaffold illustrates the effective interaction between hydroxyapatite and the mentioned bonds in collagen. The N–H deformation at 1350–1500 cm^{-1} for the amide II and the amide III bands confirms also the successful bonding of collagen and hydroxyapatite The comparison of NLcp

and HA/Coll-NLcp spectra indicates that the adding NLcp to HA/Coll scaffold led to the removal of the peak at the range of 1700–1750 cm^{-1} [i.e. the peak of 1738.06 cm^{-1} that was assigned to C=O symmetry stretching vibration].

Moreover, the range change of the peaks and their intensity in the HA/Coll-NLcp spectrum than HA/Coll and NLcp spectra [especially, the peak of 3409.37 cm^{-1} (N–H stretching vibration) and

1996.16 cm^{-1} (C≡C symmetry stretching vibration)], are attributed to chemical interactions between the HA/Coll and NLcp.

The deformation of some peaks at the range of 500–1650 cm^{-1} and the appearance of the peak at 873.99 cm^{-1} for HA/Coll-NLcp spectrum, compared to HA/Coll, also indicates the interaction of NLcp with polymer chains via C—O asymmetric/symmetric stretching vibrations, the —CH$_3$ and —CH$_2$ bonds, as well as C—H and C≡C aromatic stretching [37,38].

Followed by, the influence of NLcp inclusion on the compression strength of the HA/Coll-based scaffolds was assessed (Fig. 2B). Accordingly, the steep slope in the HA/Coll-NLcp scaffold could be interpreted as a stiffer scaffold that can be due to the existence of NLcp (PLGA-Lycopene nanoparticles) in the scaffold structure and better interaction of PLGA with polymer chains for creating a stronger network. Likewise, a low slope is related to the lower tensile strength that led to an easily deformed scaffold. Given that the property of composites is the combination of the properties of their constituent materials, it is expected that adding NLcp to the HA/Coll scaffold leads to an increase in the elastic deformation range of the scaffold and consequently prevents its entry into the plastic region (i.e. permanent deformation).

Based on the results, the elasticity modulus or Young's modulus of HA/Coll and HA/Coll-NLcp scaffolds (which expresses the stiffness of the materials) was 62 ± 7 MPa and 98 ± 3 MPa, respectively (p < 0.001). The yield stress (maximum tolerable stress by the materials before entering the plastic region) for these two scaffolds was also 2.90 ± 0.08, 4.8 ± 0.05 MPa, respectively (p < 0.05, Table 1).

Fig. 2(C and D) demonstrates the SEM images of the designed scaffolds. Lycopene nanoparticles were indicated as white particles on the polymeric substrate (Fig. 2C). The agglomeration or accumulation of the particles observes in some parts, which can be owing to the small surface areas and higher surface energies of these particles [45]. The comparison of morphological images illustrates although both scaffolds possess porosity related to the removal of solvent molecules, however higher porosity was assigned to HA/Coll-NLcp scaffold. This can be due to the existence of NLcp solution when preparing the composite solution and the interaction of NLcp with polymer chains, and consequently the creation of a more integrated network and compression strength of scaffold. Moreover, the improvement of scaffold wells and proper distribution of nanoparticles on the scaffold network was observed which can be a reason to avoid stress concentration on one side of the scaffold and consequently improve mechanical properties.

The degradation rate of scaffolds was also evaluated by measuring their weight loss in PBS as a function of time (90 days of immersion). The degradation diagram of the scaffolds have been shown in Fig. 2E. Based on the results, the linear-like pattern of HA/coll degradation not much has changed by when it is doped with NLcp powder. However, the NLcp influenced HA/coll-based scaffold degradation rate. As shown in this Figure, at 15 days, the mass loss percentages were 23.2% ± 1.01 and 19.10% ± 1.3 in the HA/Coll and HA/Coll/NLcp scaffolds, respectively. During the degradation process of scaffolds, the mass loss rate increased so that after 90 days, the mass remaining percentages for these two scaffolds were 25.4% ± 1.2% and 20.3% ± 1.0% respectively. Generally, HA/Coll-NLcp scaffold showed similar degradation behavior as HA/Coll scaffold, but with a gentler rate of degradation that can be due to the

bonding of NLcp to polymer chains in the HA/Coll-based scaffold structure.

Moreover, in-vitro cytotoxicity analysis also indicated that the HA/Coll-NLcp scaffold was increased active cells than the HA/Coll scaffold (p < 0.05) (Fig. 2F). Such that, a higher absorbance demonstrates the existence of more cells or that they are metabolizing [46], that can be due to the surface morphology and/or excellent bioactivity of NLcp.

3.3. Determination of hEnMSC and exosome characterization

Based on the results of flow cytometric analysis, the standardized culture of hEnMSC has led to the expression of surface markers of MSCs and endometrial following the serial passage (Fig. 3A). Accordingly, CD90 and CD105 demonstrated a higher expression level of >99%. The CD146 was also expressed on the surface of hEnMSCs, at higher levels than 86%. Notably, the expression of endothelial and hematopoietic markers CD31 and CD34 was obtained lower than 3% (i.e. 2.86% and 1.30% respectively).

Moreover, the analyses of the cellular morphology by phase contrast microscopy confirmed the same fibroblast-like and spindle-shaped morphology for the hEnSCs (Fig. 3B).

After treating with the induction medium which contains dexamethasone, IBMX (3-isobutyl-1-methylxanthine) for 2 weeks, the staining was carried out with Oil red O solution to confirm HEnMSC differentiation into adipose cells (Fig. 3C and D). As observed in Fig. 3C, the intracellular fat vacuoles are colored red.

hEnMSCs differentiation into osteoblast cells in the induction medium containing dexamethasone was also confirmed by Alizarin red S staining protocol. Accordingly, the good color of the cells indicates calcium deposition in bone cells, while the control sample is not colored due to the absence of calcium (Fig. 3E and F).

Furthermore, the Bradford assay and the determination of the concentration of exosomes via a standard curve illustrated a 150 μg/μL concentration. The result of the SEM (scanning electron microscope) image also demonstrated that hEnMSC-derived exosomes possess a spherical shape with a mean diameter of 104.3 nm ± 0.023 (Fig. 3G) confirming the structure and size of these vesicles [47]. While, the mean diameter obtained from DLS analysis was 421 nm (Fig. 3H), which can be owing to the aggregation of exosomes in the aqueous medium of DLS analysis. The aggregation process also observes in the SEM image (red circle).

The results of the Western blot assay also confirmed the presence of hEnMSC-derived exosomes (CD63) (Fig. 3I).

Cumulative release (%) of exosomes from the scaffold also indicated a burst release behavior between the days of 15–30 (gtadient: 61.39°) and in following a gentler release profile on the days 30–90 (gtadient in 30–60 days: 12.14°, gtadient of 60–90 days: 56.16°) (Fig. 3J). It can be related to the dissociation of polymer chains, so that the increase in the degradation rate of the scaffold which accelerates by beginning with the fifteenth day led to a higher release rate of the exosomes. However, before 15 days, a slower release behavior reports for samples due to the strength of the scaffold network and less hydrolysis of its constituent polymers. After 30 days, the release rate decreased (between 30 and 90) so that the release profile of exosomes possessed a gentle slope, again correlated with relative hydrolysis of the polymeric network.

3.4. Animal study

A total of 30 histological samples (3 histological sections for each sample) were analyzed in the current study. On days 45 and 90 post-implantation, the histological sections were blindly evaluated, scored, and reported (Fig. 4I and II) through an expert pathologist according to the new system scoring for bone regeneration. Newly

Table 1
The mechanical properties of the designed scaffolds.

| Sample	Elasticity modulus (MPa)	σ yield	ε failure (%)
HA/Coll	62 ± 7	2.9 ± 0.08	5.048 ± 0.14
HA/Coll-NLycopene	98 ± 3	4.8 ± 0.05	8.99 ± 0.03
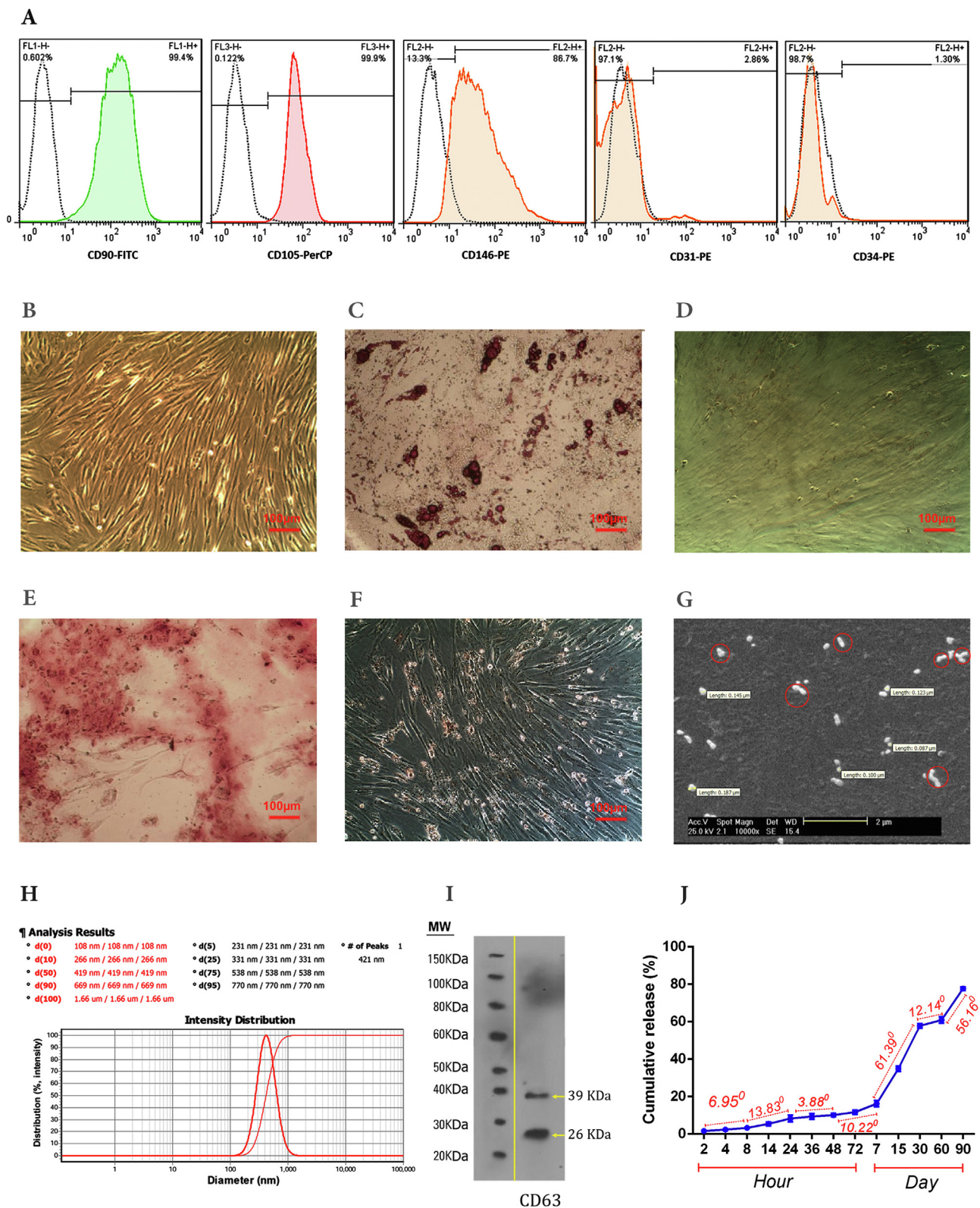
Fig. 3. Flow cytometric images (A), the analyses of the cellular morphology by phase contrast microscopy (B), evaluation of HEnMSC differentiation into adipose cells (C) and control group (D) with Oil red O solution, evaluation of hEnMSCs differentiation into osteoblast cells (E) and control sample (F) by Alizarin red S staining protocol, SEM images of hEnMSC-derived exosomes (G), DLS analysis (H), Western blot assay (I), the cumulative release (%) of exosomes from the scaffold (J).

formed bone, cartilage, and fibrous tissue with the mean histo-pathological scores of 18.60 ± 2.30 and 21 ± 2.54, 23.80 ± 2.38 were found in the defect, HA/Coll scaffold, and HA/Coll-NLcp scaffold groups. Likewise, newly formed bone and cartilage tissue with the mean histopathological scores of 28 ± 1.58 and 32 ± 1.58, 23.80 ± 2.38 were found in the HA/Coll scaffold + exosome and HA/Coll/NLcp scaffold + exosome groups on days 45 post-implantation.

All treatment groups significantly showed lower mean histo-logical scores than that of the control group on days 45 and 90 post-treatment. The HA/Coll-NLcp scaffold + exosome group significantly showed higher histological scores than those of the HA/Coll scaffold + exosome ($p = 0.038$), defect ($p < 0.001$), scaffold ($p < 0.001$), and HA/Coll-NLcp scaffold ($p < 0.001$) groups on day 45 post-implantation. In addition, a significant difference was
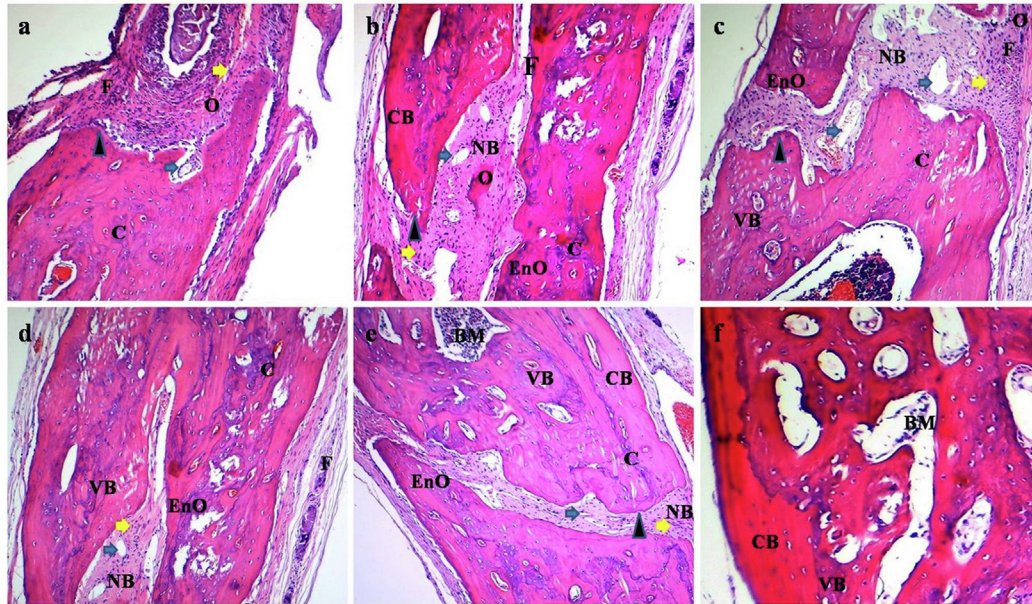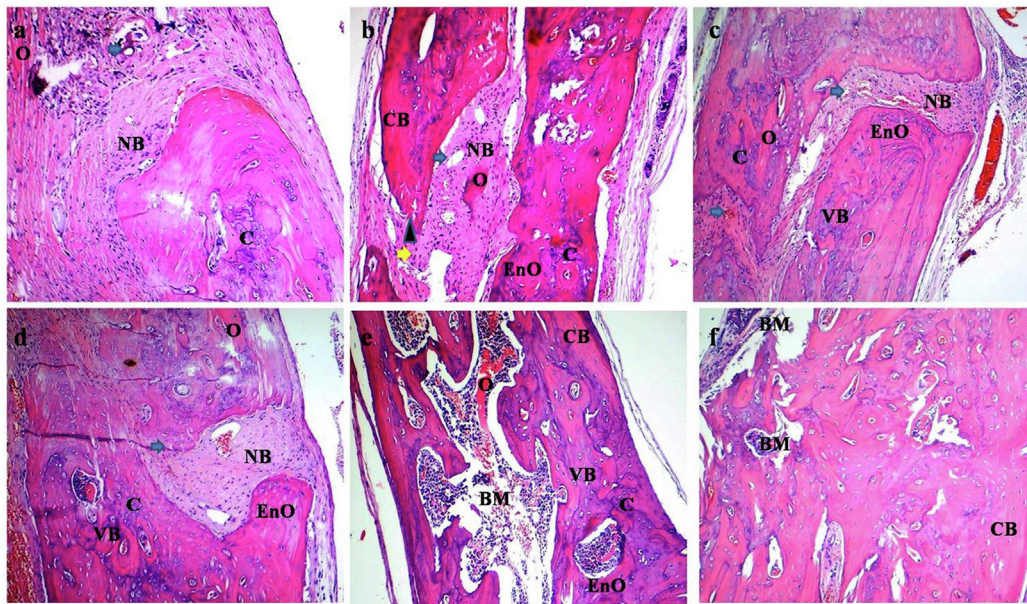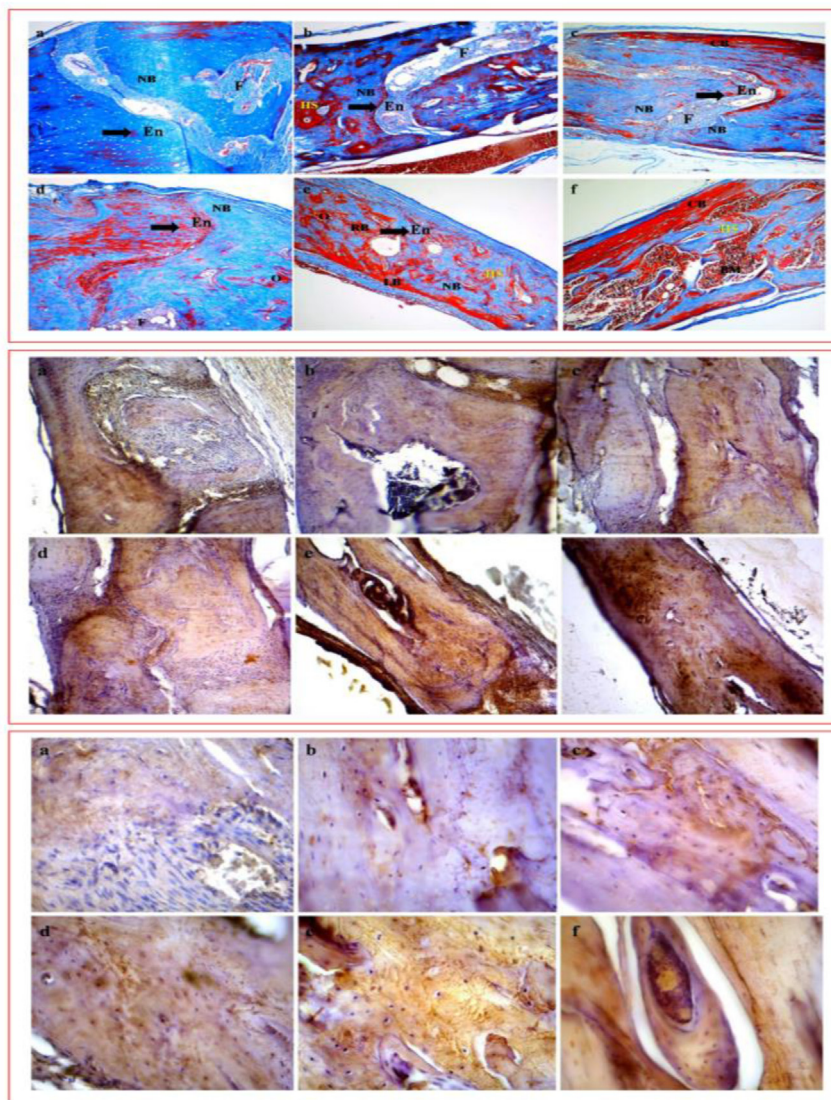

Fig. 4. Histopathological findings in the defect (a), HA/Coll scaffold (b), HA/Coll-NLcp scaffold (c), HA/Coll scaffold + exosome (d), HA/Coll-NLcp scaffold + exosome (e), and the control (f) groups on day 45 post-treatment (I) and day 90 post-treatment (II); Vessels (blue arrow), F: (fibrous), osteoblast (yellow arrow), line of the defect (arrowhead), new bone (NB), osteoid (O), cortical bone (CB), endochondral ossification (EnO), C: cartilage (C), BM: bone marrow, and woven bone (WB) (H&E Staining).

Fig. 5. (I) Masson trichrome staining [in the defect (a), HA/Coll scaffold (b), HA/Coll-NLcp scaffold (c), HA/Coll scaffold + exosome (d), HA/Coll-NLcp scaffold + exosome (e), and the control (f) groups on day 90 post-treatment, new bone (NB), osteoid (O), cortical bone (CB), Haversian system (HS), endochondral ossification (EnO), BM: bone marrow, and replaced bone (RB)]. (II) Immunohistochemistry staining, the positive immunoreactivity for osteocalcin is observed with brown color [in the defect (a), HA/Coll scaffold (b), HA/Coll-NLcp scaffold (c), HA/Coll scaffold + exosome (d), HA/Coll-NLcp scaffold + exosome (e), and the control (f) groups on day 45 post-treatment]. (III) Immunohistochemistry staining at high magnification, the positive immunoreactivity for osteocalcin is observed with brown color [in the defect (a), HA/Coll scaffold (b), HA/Coll-NLcp scaffold (c), HA/Coll scaffold + exosome (d), HA/Coll-NLcp scaffold + exosome (e), and the control (f) groups on day 45 post-treatment].

Table 2
The mean percentage of osteocalcin protein expression in various groups.

Groups	Mean on day 45 post-treatment	SD	Mean on day 90 post-treatment	SD
Defect	20.20^c	5.16	26.60^a	4.03
HA/Coll scaffold	25.80b^c	4.60	31.60^a	3.64
HA/Coll-NLcp scaffold	29.40^b	4.77	32.60^a	3.64
HA/Coll scaffold + exosome	29.80^b	2.94	32.40^a	3.57
HA/Coll-NLcp scaffold + exosome	38.40^a	3.50	27.80^a	3.19
Control	40.80^a	3.27	28.20^a	5.21

The uncommon letter in each column showed a significant difference statistically at $p < 0.05$.

observed between the HA/Coll scaffold + exosome group with the HA/Coll-NLcp scaffold ($p = 0.027$), HA/Coll scaffold ($p < 0.001$), and defect ($p < 0.001$) groups in terms of the histological score on day 45 post-implantation. A significant difference was also found in the HA/Coll-NLcp scaffold group and defect group ($p = 0.004$) respected to the mean histological score on day 45 post-treatment.

On day 90 post-treatment, the highest histological score was detected in the control group (39 ± 0.7), followed by the HA/Coll-NLcp scaffold + exosome (36 ± 1.58), the HA/Coll scaffold + exosome (31.4 ± 1.14), the HA/Coll-NLcp scaffold (29.4 ± 1.14), the HA/Coll scaffold (28.2 ± 1.30), and the defect groups (24.6 ± 1.51).

The HA/Coll-NLcp scaffold + exosome group significantly showed higher histological scores than those of the HA/Coll scaffold + exosome ($p < 0.001$), defect ($p < 0.001$), HA/Coll scaffold ($p < 0.001$), and HA/Coll-NLcp scaffold ($p < 0.001$) groups on day 90 post-implantation. In addition, a significant difference was seen between the HA/Coll scaffold + exosome group with the scaffold ($p = 0.006$), and defect ($p < 0.001$) groups in terms of the histological score on day 90 post-implantation. A significant difference was also found in the scaffold group and defect group ($p = 0.002$) respected to the mean histological score on day 90 post-treatment.

Masson trichrome staining also confirmed the histological variations in different groups (Fig. 5I). New bone formation and fibrocartilage tissues are detectable by Masson trichrome staining.

Based on these results, it seems that the scaffolds containing the exosome can promote the regeneration of bones through transferring internal cargos of this nano-biostructure and lead to the control in targeted cell signaling pathways [48,49]. In this field, the reports indicated that the use of exosomes can activate the cascades of BMP/Smad, Wnt/β-catenin and PI3K/AKT, resulting in the recruitment of stem cells to the bone defect site, and subsequently bone regeneration [50–52]. These reports can confirm our result for the exosome-containing scaffold. Moreover, the nano lycopene

can improve the functions of exosomes and in terms of the function, turn them into enriched exosomes, so that their delivery to the targeted sites is effectively maximized.

To evaluate bone formation or osteogenesis induction, immunostaining for osteocalcin (osteogenic-related protein) was performed on day 45 post-treatment (Fig. 5 II and III, Table 2). Notably, osteocalcin as the most abundant protein produced by osteoblasts was selected for this study [48].

The control and HA/Coll-NLcpscaffold + exosome groups indicated a higher mean percentage expression of osteocalcin compared to the other groups on day 45 post-treatment.

The lowest mean percentage of osteocalcin was detected in the defect group on day 45 post-treatment. The studies also illustrate that exosomes can regenerate bone defects via bone resorption suppression, and lead to increased activation of signaling pathways and osteogenesis effectiveness [53,54].

Generally, the microscopic findings (H & E, Masson trichrome staining, and IHC) demonstrate that bone regeneration, in the combination of HA/Coll/NLcp scaffold and exosome group is started faster than those of other groups. Indeed, the use of the exosome in the scaffold network can lead to the regulation of immune responses and inhibition of osteoclast activity [50,51]. Our results also
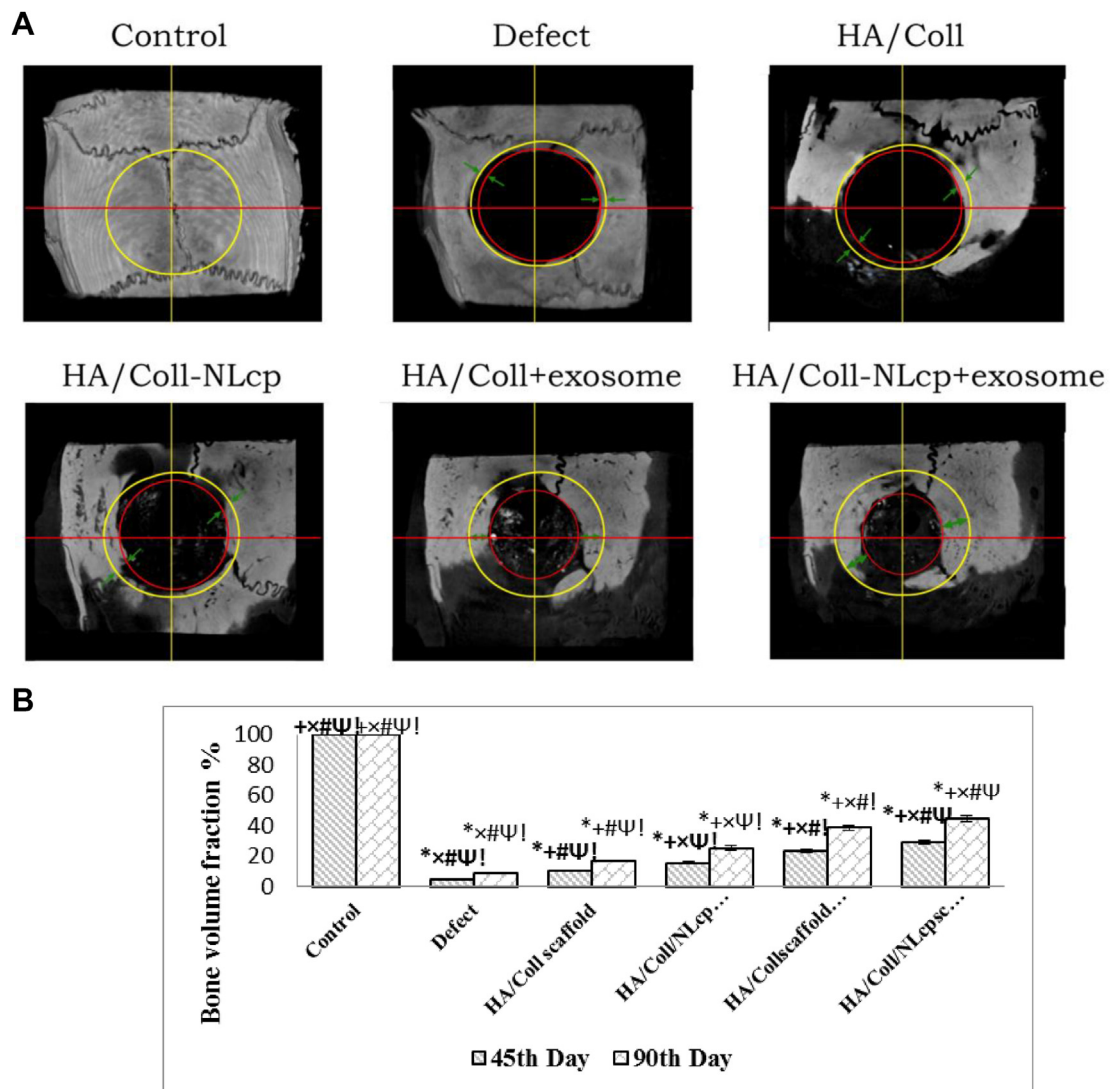

Fig. 6. (A). Micro-Computed Tomography of rat calvaria in 90th days (B). Bone volume fraction (%) in 45 and 90 days.

Table 3
The mean BVF for the studied groups, on the 90th day (Mean ± SD).

Group	90th day
Control	100.00 ± 0.00
Defect	8.33 ± 0.61
HA/Coll scaffold	17.11 ± 0.87
HA/Coll-NLcp scaffold	25.31 ± 2.78
HA/Coll scaffold + exosome	38.54 ± 3.39
HA/Coll-NLcp scaffold + exosome	44.69 ± 3.90

demonstrated that NLcp plays an important role in improving the function of exosomes for inducing osteogenesis.

There was no significant difference between all groups in terms of osteocalcin expression on day 90 post-treatment. These findings can be explained by in fact that due to the regeneration process and osteoblast activity being started later in the defect and scaffold alone groups the osteoblast activity and osteocalcin expression are continued. Bakhtiarimoghadam et al., (2021) showed that by finishing the regeneration process and osteoblast activity the osteocalcin expression is also slowed [49].

3.5. The analysis of Micro-CT images

To study bone formation on the scaffolds, the scaffolds were implanted in the rat skull-defect model for 90 days. Afterward, Micro-CT images of all groups were taken using an X-ray Micro-Computed Tomography. Fig. 6 (A) indicates the 3D images of the implanted scaffolds. The lines in this Figure demonstrate the new bone mineral formation zone within the scaffolds after 90 days. Based on the results, after skull bone defect induction, the mean BVF at 90 days decreased for all groups compared to the control group (p < 0.05, Table 3, Fig. 6B). While the mean BVF at both days increased for all groups compared to defect group (p < 0.05). The NLcp or exosome-treated scaffolds (i.e. HA/Coll-NLcp scaffold and HA/Coll scaffold + exosome) and HA/Coll-NLcp scaffold also led to an increase in the mean BVF on 90 days, compared to HA/Coll scaffold (1.47-fold, 2.25-fold and 2.61-fold, respectively) (p < 0.05). The comparison of results illustrated that the existence of only exosome or its combination of NLcp, in the scaffold network can promote the mean BVF compared with NLcp (i.e. HA/Coll-NLcp) (1.5-fold and ~1.8-fold, respectively) (p < 0.05). However, the scaffold containing NLcp + exosome demonstrated a 26.35% increase in mean BVF compared to exosome (i.e. HA/Coll scaffold + exosome).

4. Conclusion

In this study, HA-Coll scaffolds containing NLcp and exosome were fabricated successfully by the freeze-drying method. To this end, the first lycopene (as biomolecule) was loaded into PLGA and characterized, and then mixed with the polymer solution to design HA/Coll- NLcp scaffolds. Afterward, The designed scaffolds were covered by hEnMSC-derived exosomes to assess the role of NLcp and exosomes in stem cell proliferation and its differentiation into osteoblast cells. Then, the results were confirmed by DLS, SEM, flow cytometric, Western blot assay, Hematoxylin and eosin staining, immunohistochemical, and micro-CT, after 45 and 90 days. Accordingly, the study of the rat skull-defect model on 54 male Sprague–Dawley rats (12-weeks old) indicated, although the existence of NLcp in the scaffold network can improve cell differentiation and increase mean BVF compared to HA/Coll scaffold up to 1.47-fold. However, the mean BVF increased up to 2.82-fold when the exosome is covered on the HA/Coll-NLcp scaffold. It seems that a combination of bioactive materials (such as lycopene or nano-

lycopene) with biological agents (such as exosomes) can play an important role in stem cell differentiation into targeted tissues.

Declaration of competing interest

The authors declare that they have no competing interests.

Acknowledgements

References

[1] Zhao Y, Liu J, Zhang M, He J, Zheng B, Liu F, et al. Use of silver nanoparticle–gelatin/alginate scaffold to repair skull defects. Coatings 2020;10: 948. https://doi.org/10.3390/coatings10100948.
[2] Pişkin E, Işoğlu IA, Bölgen N, Vargel I, Griffiths S, Çavuşoğlu T, et al. In vivo performance of simvastatin-loaded electrospun spiral-wound polycaprolactone scaffolds in reconstruction of cranial bone defects in the rat model. J Biomed Mater Res, Part A 2009;90:1137–51. https://doi.org/10.1002/jbm.a.32157.
[3] Wang W, Yeung KWK. Bone grafts and biomaterials substitutes for bone defect repair: a review. Bioact Mater 2017;2:224–47.
[4] Bi M, Han H, Dong S, Zhang Y, Xu W, Zhu B, et al. Collagen-coated poly(lactide-co-glycolide)/hydroxyapatite scaffold incorporated with DGEA peptide for synergistic repair of skull defect. Polymers 2018;10. https://doi.org/10.3390/polym10020109.
[5] Kneser U, Schaefer DJ, Polykandriotis E, Horch RE. Tissue engineering of bone: the reconstructive surgeon's point of view. J Cell Mol Med 2006;10:7–19.
[6] Winkler T, Sass FA, Duda GN, Schmidt-Bleek K. A review of biomaterials in bone defect healing, remaining shortcomings and future opportunities for bone tissue engineering: the unsolved challenge. Bone Joint Res 2018;7: 232–43.
[7] Nahanmoghadam A, Asemani M, Goodarzi V, Ebrahimi-Barough S. In vivo investigation of PCL/PHBV/hydroxyapatite nanocomposite scaffold in regeneration of critical-sized bone defects. Fibers Polym 2021;22:2507–16.
[8] Nahanmoghadam A, Asemani M, Goodarzi V, Ebrahimi-Barough S. Design and fabrication of bone tissue scaffolds based on PCL/PHBV containing hydroxyapatite nanoparticles: dual-leaching technique. JBMR-Part A 2021;109: 981–93.
[9] Hollister SJ. Porous scaffold design for tissue engineering. Nat Mater 2005;4: 518–24.
[10] Huh J, Lee J, Kim W, Yeo M, Kim G. Preparation and characterization of gelatin/α-TCP/SF biocomposite scaffold for bone tissue regeneration. Int J Biol Macromol 2018;110:488–96.
[11] Lai Y, Cao H, Wang X, Chen S, Zhang M, Wang N, et al. Porous composite scaffold incorporating osteogenic phytomolecule icariin for promoting skeletal regeneration in challenging osteonecrotic bone in rabbits. Biomaterials 2018;153:1–13.
[12] Yang L, Ge L, van Rijn P. Synergistic effect of cell-derived extracellular matrices and topography on osteogenesis of mesenchymal stem cells. ACS Appl Mater Interfaces 2020;12:25591–603.
[13] Sartori M, Giavaresi G, Parrilli A, Ferrari A, Aldini NN, Morra M, et al. Collagen type I coating stimulates bone regeneration and osteointegration of titanium implants in the osteopenic rat. Int Orthop 2015;39:2041–52.
[14] Astete CE, Sabliov CM. Synthesis and characterization of PLGA nanoparticles. J Biomater Sci Polym Ed 2006;17:247–89.
[15] Cui H, Liu Y, Deng M, Pang X, Zhang P, Wang X, et al. Synthesis of biodegradable and electroactive tetraaniline grafted poly (ester amide) copolymers for bone tissue engineering. Biomacromolecules 2012;13:2881–9.
[16] Izadyari Aghmiuni A, Ghadi A, Azmoun E, Kalantari N, Mohammadi I, Hemati Kordmahaleh H. Electrospun polymeric substrates for tissue engineering: viewpoints on fabrication, application, and challenges. Electrospinning - Mater Technol Future 2022. https://doi.org/10.5772/intechopen.102596.
[17] Barnes CP, Sell SA, Boland ED, Simpson DG, Bowlin GL. Nanofiber technology: designing the next generation of tissue engineering scaffolds. Adv Drug Deliv Rev 2007;59:1413–33.
[18] Sell SA, Wolfe PS, Garg K, McCool JM, Rodriguez IA, Bowlin GL. The use of natural polymers in tissue engineering: a focus on electrospun extracellular matrix analogues. Polymers 2010;2:522–53. https://doi.org/10.3390/polym2040522.
[19] Khanmohammadi M. Encapsulation of stem cells. In: Sefat F, Farzi G, Mozafari M, editors. Principles of biomaterials encapsulation. Woodhead Publishing; 2023. p. 481–524.
[20] Mano JF, Silva GA, Azevedo HS, Malafaya PB, Sousa RA, Silva SS, et al. Natural origin biodegradable systems in tissue engineering and regenerative

medicine: present status and some moving trends. J R Soc Interface 2007;4: 999—1030.

[21] Choi JS, Lee SW, Jeong I, Bae S-H, Min BC, Youk JH, et al. Effect of organo-soluble salts on the nanofibrous structure of electrospun poly (3-hydroxybutyrate-co-3-hydroxyvalerate). Int J Biol Macromol 2004;34: 249—56.

[22] Thomas V, Dean DR, Jose MV, Mathew B, Chowdhury S, Vohra YK. Nano-structured biocomposite scaffolds based on collagen coelectrospun with nanohydroxyapatite. Biomacromolecules 2007;8:631—7.

[23] Suganya S, Venugopal J, Ramakrishna S, Lakshmi BS, Giri Dev VR. Herbally derived polymeric nanofibrous scaffolds for bone tissue regeneration. J Appl Polym Sci 2014;131. n/a-n/a. doi:10.1002/app.39835.

[24] Lee CH, Huang YL, Liao JF, Chiou WF. Ugonin K-stimulated osteogenesis in-volves estrogen receptor-dependent activation of non-classical Src signaling pathway and classical pathway. Eur J Pharmacol 2012;676:26—33. https://doi.org/10.1016/j.ejphar.2011.12.001.

[25] Xiao HH, Gao QG, Zhang Y, Wong KC, Dai Y, Yao XS, et al. Vanillic acid exerts oestrogen-like activities in osteoblast-like UMR 106 cells through MAP kinase (MEK/ERK)-mediated ER signaling pathway. J Steroid Biochem Mol Biol 2014;144:382—91. https://doi.org/10.1016/j.jsbmb.2014.08.002.

[26] Don MJ, Lin LC, Chiou WF. Neobavaisoflavone stimulates osteogenesis via p38-mediated up-regulation of transcription factors and osteoid genes expression in MC3T3-E1 cells. Phytomedicine 2012;19:551—61. https://doi.org/10.1016/j.phymed.2012.01.006.

[27] Srivastava S, Bankar R, Roy P. Assessment of the role of flavonoids for inducing osteoblast differentiation in isolated mouse bone marrow derived mesen-chymal stem cells. Phytomedicine 2013;20:683—90. https://doi.org/10.1016/j.phymed.2013.03.001.

[28] Bengi V U, Saygun I, Bal V, Ozcan E, Kose Ozkan C, Torun D, et al. Effect of antioxidant lycopene on human osteoblasts. Clin Oral Invest 2022. https://doi.org/10.1007/s00784-022-04789-z.

[29] Rahimi A, Nahanmoghadam A, Ai J, Gholami N, Ebrahimi-Barough R, Ebra-himi-Barough S. Motor neurons differentiation of encapsulated human endometrial stem cells in collagen without HLA-DR expression. Journal of Applied Tissue Engineering 2019;6:6—16.

[30] Shang F, Yu Y, Liu S, Ming L, Zhang Y, Zhou Z, et al. Advancing application of mesenchymal stem cell-based bone tissue regeneration. Bioact Mater 2021;6: 666—83. https://doi.org/10.1016/j.bioactmat.2020.08.014.

[31] Maqsood M, Kang M, Wu X, Chen J, Teng L, Qiu L. Adult mesenchymal stem cells and their exosomes: sources, characteristics, and application in regenerative medicine. Life Sci 2020;256:118002. https://doi.org/10.1016/j.lfs.2020.118002.

[32] Li X, Liu H, Niu X, Yu B, Fan Y, Feng Q, et al. The use of carbon nanotubes to induce osteogenic differentiation of human adipose-derived MSCs in vitro and ectopic bone formation in vivo. Biomaterials 2012;33:4818—27.

[33] Yang X, Li Y, Liu X, Zhang R, Feng Q. In vitro uptake of hydroxyapatite nanoparticles and their effect on osteogenic differentiation of human mesenchymal stem cells. Stem Cell Int 2018;2018.

[34] Heidari-Keshel S, Rezaei TM, Ai J, Soleimani M, Ghanbari Z, Baradaran-Rafii AR. Isolation and characterization of endometrial mesenchymal stem cells and the evaluation of surface markers in comparison to bone marrow mesenchymal stem cells. Sci J Iran Blood Transfus Organ 2015;11.

[35] Sinha K, Das Saha P, Datta S. Extraction of natural dye from petals of Flame of forest (Butea monosperma) flower: process optimization using response surface methodology (RSM). Dyes Pigments 2012;94:212—6.

[36] López-Cervantes J, Sánchez-Machado DI, Valenzuela-Sánchez KP, Núñez-Gastélum JA, Escárcega-Galaz AA, Rodríguez-Ramírez R. Effect of solvents and methods of stirring in extraction of lycopene, oleoresin and fatty acids from over-ripe tomato. Int J Food Sci Nutr 2014;65:187—93. https://doi.org/10.3109/09637486.2013.839630.

[37] Chavan JJ, Ghadage DM, Kshirsagar PR, Kudale SS. Optimization of extraction techniques and RP-HPLC analysis of antidiabetic and anticancer drug

mangiferin from roots of saptarangi (Salacia chinensis L.). J Liq Chromatogr Relat Technol 2015;38:963—9. https://doi.org/10.1080/10826076.2014.999199.

[38] Rahimpour S, Taghian Dinani S. Lycopene extraction from tomato processing waste using ultrasound and cell-wall degrading enzymes. J Food Meas Char 2018;12:2394—403. https://doi.org/10.1007/s11694-018-9856-7.

[39] Bhutada PR, Jadhav AJ, Pinjari DV, Nemade PR, Jain RD. Solvent assisted extraction of oil from Moringa oleifera Lam. seeds. Ind Crops Prod 2016;82: 74—80.

[40] Suganya T, Renganathan S. Optimization and kinetic studies on algal oil extraction from marine macroalgae Ulva lactuca. Bioresour Technol 2012;107: 319—26.

[41] Lin W, Garnett MC, Davies MC, Bignotti F, Ferruti P, Davis SS, et al. Preparation of surface-modified albumin nanospheres. Biomaterials 1997;18:559—65. https://doi.org/10.1016/S0142-9612(96)00176-7.

[42] Abelha TF, Phillips TW, Bannock JH, Nightingale AM, Dreiss CA, Kemal E, et al. Bright conjugated polymer nanoparticles containing a biodegradable shell produced at high yields and with tuneable optical properties by a scalable microfluidic device. Nanoscale 2017;9:2009—19. https://doi.org/10.1039/C6NR09162H.

[43] Ghorbani M, Mahmoodzadeh F, Nezhad-Mokhtari P, Hamishehkar H. A novel polymeric micelle-decorated Fe 3 O 4/Au core—shell nanoparticle for pH and reduction-responsive intracellular co-delivery of doxorubicin and 6-mercaptopurine. New J Chem 2018;42:18038—49.

[44] Phan QT, Le MH, Le TTH, Tran THH, Xuan PN, Ha PT. Characteristics and cytotoxicity of folate-modified curcumin-loaded PLA-PEG micellar nano sys-tems with various PLA: PEG ratios. Int J Pharm 2016;507:32—40.

[45] Šupová M. Problem of hydroxyapatite dispersion in polymer matrices: a re-view. J Mater Sci Mater Med 2009;20:1201—13. https://doi.org/10.1007/s10856-009-3696-2.

[46] Kim HW, Kim HE, Salih V. Stimulation of osteoblast responses to biomimetic nanocomposites of gelatin-hydroxyapatite for tissue engineering scaffolds. Biomaterials 2005;26:5221—30. https://doi.org/10.1016/j.biomaterials.2005.01.047.

[47] Wang J, Yao Y, Wu J, Li G. Identification and analysis of exosomes secreted from macrophages extracted by different methods. Int J Clin Exp Pathol 2015;8:6135—42.

[48] Zoch ML, Clemens TL, Riddle RC. New insights into the biology of osteocalcin. Bone 2016;82:42—9.

[49] Gharati G, Shirian S, Sharifi S, Mirzaei E, Bakhtirimoghadam B, Karimi I, et al. Comparison capacity of collagen hydrogel and collagen/strontium bioglass nanocomposite scaffolds with and without mesenchymal stem cells in regeneration of critical sized bone defect in a rabbit animal model. Biol Trace Elem Res 2022;200(7):3176—86. https://doi.org/10.1007/s12011-021-02909-6. Epub 2021 Sep 27. PMID: 34570341.

[50] Yang H, Cong M, Huang W, Chen J, Zhang M, Gu X, et al. The effect of human bone marrow mesenchymal stem cell-derived exosomes on cartilage repair in rabbits. Stem Cells Int 2022:2022.

[51] Wang D, Cao H, Hua W, Gao L, Yuan Y, Zhou X, et al. Mesenchymal stem cell-derived extracellular vesicles for bone defect repair. Membranes (Basel) 2022;12:716.

[52] Yahao G, Xinjia W. The role and mechanism of exosomes from umbilical cord mesenchymal stem cells in inducing osteogenesis and preventing osteopo-rosis. Cell Transplant 2021;30:09636897211057465.

[53] Maity S, Das F, Ghosh-Choudhury N, Kasinath BS, Ghosh Choudhury G. High glucose increases miR-214 to power a feedback loop involving PTEN and the Akt/mTORC1 signaling axis. FEBS Lett 2019;593:2261—72.

[54] Liang B, Liang J-M, Ding J-N, Xu J, Xu J-G, Chai Y-M. Dimethyloxaloylglycine-stimulated human bone marrow mesenchymal stem cell-derived exosomes enhance bone regeneration through angiogenesis by targeting the AKT/mTOR pathway. Stem Cell Res Ther 2019;10:1—11.